



Homogenization based macroscopic model of phase transformations and cyclic plasticity in pearlitic steel

Downloaded from: <https://research.chalmers.se>, 2023-09-29 08:34 UTC

Citation for the original published paper (version of record):

Andersson, B., Ahlström, J., Ekh, M. et al (2022). Homogenization based macroscopic model of phase transformations and cyclic plasticity in pearlitic steel. *Journal of Thermal Stresses*, In Press.
<http://dx.doi.org/10.1080/01495739.2022.2056557>

N.B. When citing this work, cite the original published paper.

Homogenization based macroscopic model of phase transformations and cyclic plasticity in pearlitic steel

Björn Andersson, Johan Ahlström , Magnus Ekh , and B. Lennart Josefson 

Department of Industrial and Materials Science, Chalmers University of Technology, Gothenburg, Sweden

ABSTRACT

In this contribution macroscopic modeling of phase transformations and mechanical behavior of low alloy steels are developed and investigated. Such modeling is of importance in simulations of transient thermo-mechanical processes which can cause phase transformations, examples from the railway industry include train braking induced frictional heating as well as rail grinding and welding operations. We adopt a modeling approach which includes phase transformation kinetics and individual constitutive models for the phases in combination with different homogenization methods. Algorithmic implementations of the isostrain, isostress and self-consistent homogenization methods are presented and demonstrated in finite element simulations of a laser heating experiment. Stress field results from the different homogenization methods are compared against each other and also against experimental data. The importance of including transformation induced plasticity in the modeling is highlighted, as well as the multi-phase stages of the heating and cooling.

ARTICLE HISTORY

Received 30 November 2021
Accepted 13 March 2022



KEYWORDS

Cyclic plasticity;
homogenization; multi-
phase steel; phase
transformation;
residual stress

1. Introduction

Heating and cooling of ferrous alloys can cause drastic changes to the material properties depending on both the temperature range and the heating rate. Permanent changes to the properties are caused by changes within the material microstructure, see e.g. [1]. With this knowledge, alloys and heat treatments are tailored to meet different specific needs, e.g. strength, formability or wear resistance. However, local high temperature in operations can cause the structural properties of the heat-affected region to deviate from its desired characteristics. To predict and understand the consequences of local heating events, several constitutive models and numerical simulation tools have been devised in the literature.

The underlying mechanisms occur on the micro- and macroscopic scale and consist of interacting thermal, metallurgical and mechanical phenomena. Due to this inherent complexity, much process modeling research is to varying degree application specific. Simulation of welding is one such example, well presented in e.g. the review series by Lindgren [2–4]. Other examples of process simulations include quenching, cf. [5–11], stamping, cf. [12–15], and additive manufacturing, cf. [16–20]. Simulations of local heating in railway wheels caused by braking are another example, cf. [21–26]. Even though the prime focus may differ, common for all these examples is that the

CONTACT Björn Andersson  abjorn@chalmers.se  Department of Industrial and Materials Science, Chalmers University of Technology, Gothenburg, Sweden.

© 2022 The Author(s). Published with license by Taylor and Francis Group, LLC

This is an Open Access article distributed under the terms of the Creative Commons Attribution-NonCommercial-NoDerivatives License (<http://creativecommons.org/licenses/by-nc-nd/4.0/>), which permits non-commercial re-use, distribution, and reproduction in any medium, provided the original work is properly cited, and is not altered, transformed, or built upon in any way.

material modeling is one of the most challenging and crucial aspects for the fidelity of the simulation results.

The list of works published concerning modeling of mechanical behavior caused by phase transformations in steel contains hundreds of titles and stretches over some five decades. Some examples are: Inoue and Raniecki, [27], Sjöström [28], Leblond et al. [29,30], Denis et al. [31], Fischer et al. [32], Hallberg et al. [33], Iwamoto and Tsuta [34], Mahnken et al. [35], Wolff et al. [36], and Weisz-Patrault [37]. The list of works presenting underlying mechanisms which can be accounted for in such modeling is equally long, such examples include: diffusion controlled transformations (cf. Johnson–Mehl–Avrami–Kolmogorov [38–40]), diffusionless transformation (cf. Koistinen and Marburger [41]), diffusional transformation under anisothermal conditions (cf. Scheil [42]), transformation induced plasticity (cf. Greenwood and Johnson, [43], Magee [44]), strain-induced martensitic transformation (cf. Olson and Cohen [45]), bainite transformation (cf. Bhadeshia and Edmonds [46]) and plastic inheritance (cf. Petit-Grostabussiat [47], Levitas [48], Ostwald et al. [49,50]).

The macroscopic response of a multi-phase steel can be computed by using different homogenization methods. The most high-fidelity method is to use the finite element method of a microstructure model with boundary conditions fulfilling the Hill-Mandel conditions, cf. Zohdi and Wriggers [51]. However, it is common to use more computationally efficient methods such as the Voigt assumption of uniform strain (cf. Mahnken et al. [35]), the Reuss assumption of uniform stress (cf. [52]), the Hill condition taking the arithmetic average of Voigt and Reuss (cf. [53]), the uniform work assumption (cf. [54,55]) or a mean-field homogenization approach such as the self-consistent scheme (cf. [56]). Several of these methods are evaluated by Perdahcioglu [57] in FE simulations of sheet metal forming of dual-phase steel. It is found that the choice of homogenization method gives significant influence on the resulting stress state.

The most common approach in literature to model the mechanical behavior of steel with phase transformations is to use linear mixture rules (e.g. [32]), especially those examining transient events such as quenching (e.g. [31]). Even-though the works using non-linear rules (e.g. [56]) often indicate that linear mixture rules may not be sufficient to replicate experimental material behavior. In Mahnken [35] this is investigated by using finite element simulations of a cubic cell to identify the mixture rule of the material hardening.

Inspired by findings indicating that linear mixture rules are sometimes insufficient, we examine different homogenization methods in this study. This means that material modeling of the individual phases must be performed and is done for the application of transient heating and cooling of pearlitic steel, where both austenitization and martensite formation are accounted for. The work is an extension of a previous work [26], where only the isostrain assumption was adopted, see Section 4.2. Motivated by the conclusion about the significant influence of the homogenization method in Perdahcioglu et al. [57] we also adopt the isostress assumption and the self-consistent assumption. As compared to [26], the current work is also extended by accounting for the TRIP-effect and by improving the procedure for updating internal variables as phase transformations occur. Simulation results are compared to experimental residual stresses measured after laser heating experiments in [58] and to results obtained using the linear mixture rule. The study highlights the importance of including TRIP modeling as well as choice of homogenization method.

The structure of the article is as follows; Section 2 presents how the metallurgical changes are modeled. The constitutive model for the phases is presented in Section 3. In Section 4, the adopted homogenization methods are presented together with their numerical implementation. Finally, results from finite element simulations with the different model assumptions are evaluated against data from laser heating experiments in Section 5.

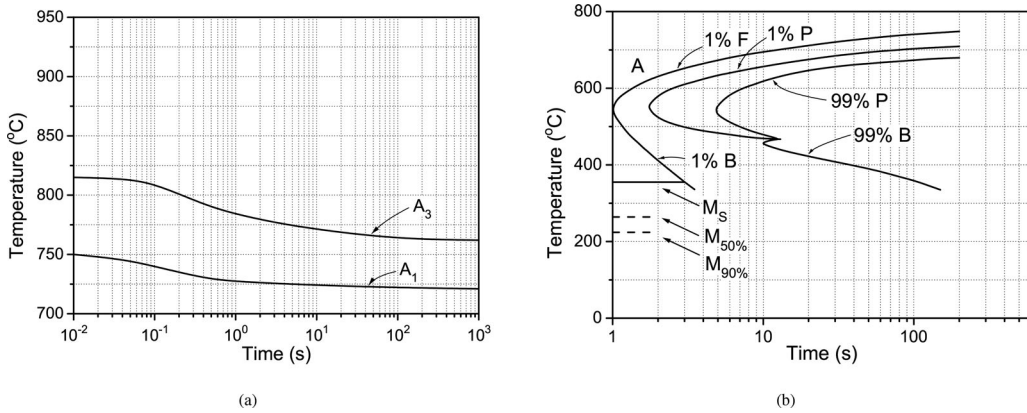


Figure 1. (a) TTA diagram describing phase transformation kinetics during austenitization at constant heating rates (reproduced from [60]). (b) IT diagram describing isothermal transformation kinetics during cooling from austenite (reproduced from [61]).

2. Phase transformations

2.1. Preliminaries

The study presented in this paper is limited to one single heating stage followed by a cooling stage of an initially fully pearlitic rail steel R260 [59] with an approximate chemical composition Fe-0.72C-0.3Si-1Mn. Thus, the material has a slightly hypo-eutectoid composition, but still exhibits a fully pearlitic microstructure after production. Hence, only the following temperature driven phase transformations are considered:

1. Pearlite into austenite during heating
2. Austenite into martensite on high cooling rates
3. Austenite into pearlite and/or ferrite and/or bainite during moderate rates

Note that this paper considers hypoeutectoid steels only, whereby cementite phase transformations are not considered. Throughout the paper, pearlite is referred to as a phase even though it is in fact a microstructure with a lamellar arrangement of ferrite and cementite.

2.2. Phase transformation kinetics

In this section we briefly describe the kinetics governing these transformations, full details are given in e.g. [26]. The following indices are used to denote the phases: austenite (a), pearlite (p), ferrite (f), bainite (b), and martensite (m). During the heating and cooling, the sum of all phase volume fractions, p_x , must equal 1:

$$\sum_x p_x = 1 \quad \text{for } x = a, p, f, b, m \quad (1)$$

To describe the kinetics of the first phase transformation, austenitization of pearlite, the IT-diagram in Figure 1(a) is used. The line A_1 is the temperature where 1% of the pearlite has transformed while A_3 is the temperature where 99% of the pearlite has transformed. For a constant temperature in the IT-diagram, the transformation kinetics of the decreasing pearlite volume fraction is described by the Johnson-Mehl-Avrami-Kolmogorov (JMAK) equation cf. [6, 62].

$$p_p(t; T) = p_p(\tilde{t}) \exp\left(-b_p(T) (t - \tilde{t})^{n_p(T)}\right) \quad (2)$$

where $n_p(T)$ is the Avrami exponent, $b_p(T)$ is the overall crystallization rate constant and \tilde{t} is the start time of heating. The nucleated austenite is then obtained as $p_a = 1 - p_p$. To handle the varying temperatures of our intended applications using the IT-diagram, the Scheil's additive rule [42] is adopted see e.g. [63].

The kinetics of the second and third phase transformations are based on the IT-diagram in [Figure 1\(b\)](#). The second phase transformation is the formation of martensite during rapid cooling of austenite, i.e. quenching, below the temperature T_{ms} . It is assumed to be diffusionless and is modeled by using the purely temperature dependent Koistinen-Marburger [41] equation:

$$p_a(T) = p_a(T_{ms}) \exp(-k_\theta (T_{ms} - T)) \quad (3)$$

where p_a is the remaining volume fraction austenite and the parameter k_θ determines the temperature dependent increase of the martensite. Using the remaining volume fraction austenite, the volume fraction of martensite can be computed as:

$$p_m(T) = p_a(T_{ms}) - p_a(T) \quad (4)$$

To facilitate FE-solver convergence during martensitic transformation a smoother evolution of very low martensite volume fractions is adopted by replacing [Equation 3](#) with a tangens hyperbolicus function to compute the volume fraction during the initiation of martensite.

Under low to moderate cooling rates, austenite transforms into ferrite, pearlite, and/or bainite which is the third of the phase transformations considered in this paper. As these transformations are of diffusive nature, we again use the JMAK equation and Scheil's additive rule together to describe the transformation kinetics shown in [1\(b\)](#). This gives that the volume fractions of pearlite, ferrite, and/or bainite increase according to:

$$p_x(t; T) = p_x(\hat{t}) + p_a(\hat{t}) \left(1 - \exp(-b_x(T) (t - \hat{t})^{n_x(T)})\right) \quad \text{for } x = f, p, b \quad (5)$$

where \hat{t} is the time at which the cooling starts, b_x is the crystallization rate constant, and n_x the Avrami exponent for each phase. From the austenite volume fraction at the start of the cooling, $p_a(\hat{t}) = p_a(T_{ms})$, the remaining austenite phase fraction, $p_a(t; T)$, is computed according to:

$$p_a(t; T) = p_a(\hat{t}) - \sum_x (p_x(t; T) - p_x(\hat{t})) \quad \text{for } x = f, p, b \quad (6)$$

In the numerical examples studied in this paper the bainitic phase transformation will not occur. Therefore it is not considered in the remaining of the paper.

3. Constitutive model for individual phases

3.1. Preliminaries

The constitutive model for the mixture of phases in the steel, i.e. the multi-phase steel, is assumed to be obtained from homogenization of individual constitutive models for the phases. The constitutive models are run in parallel and the homogenization method accounts for the phase volume fractions of the current time step. Phases which have yet to materialize, i.e. $p_x = 0$, are assumed to not accumulate hardening or plastic strain, thus behaving linear elastic. As a new phase starts to nucleate during transformation from its parent phase, the stress-strain state enforced by the homogenization method is imposed and the constitutive response hardens accordingly. For phases reborn, e.g. austenite transforming back into pearlite, the internal variable history is, for simplicity, maintained, i.e. reborn phases are assumed not to have so called virgin material state.

However, as the examples presented in this study considers rapid cooling rates and no reheating, this simplification does not effect the final results.

3.2. Kinematics and elasticity

For all phases x in the material, we assume that the total strain ϵ_x is additively decomposed as (see e.g. [35]):

$$\epsilon_x = \epsilon_x^e + \epsilon_x^{th} + \epsilon_x^{tv} + \epsilon_x^p + \epsilon_x^{tp} \quad (7)$$

where ϵ_x^e is the elastic strain, ϵ_x^{th} the thermal expansion strain, ϵ_x^{tv} the transformation strain, ϵ_x^p the plastic strain, and ϵ_x^{tp} the strain due to transformation induced plasticity (TRIP). Note that the TRIP strain is implemented only for the austenite and martensite constitutive models ($x=a$ and $x=m$). The elastic strain governs the stress and we assume linear isotropic elasticity by adopting Hooke's law:

$$\sigma_x = \mathbf{E}_x^e : \epsilon_x^e \quad \text{with} \quad \mathbf{E}_x^e = 2 G_x \mathbf{I}_{dev} + K_{x,b} \mathbf{I} \otimes \mathbf{I} \quad (8)$$

with the fourth order deviatoric identity tensor $\mathbf{I}_{dev} = \mathbf{I} - 1/3 \mathbf{I} \otimes \mathbf{I}$, the fourth order identity tensor \mathbf{I} and the second order identity tensor \mathbf{I}^1 . Furthermore, the material parameters for elasticity are the shear modulus G_x and bulk modulus $K_{x,b}$. The stress can be decomposed into a deviatoric and a volumetric part $\sigma = \sigma_{dev} + 1/3 \sigma_{vol} \mathbf{I}$ with:

$$\sigma_{x,dev} = \mathbf{I}_{dev} : \sigma_x = 2 G_x \epsilon_{x,dev}^e \quad \text{and} \quad \sigma_{x,vol} = \mathbf{I} : \sigma_x = 3 K_{x,b} \epsilon_{x,vol}^e \quad (9)$$

The thermal expansion strain for the phases is assumed to be linear isotropic:

$$\epsilon_x^{th} = \alpha_x \Delta T \mathbf{I} \quad (10)$$

where ΔT is the temperature increase from a reference temperature T_0 and α_x is the thermal expansion factor. The initial density of the material is ρ_0 while for each phase the density is assumed to be ρ_x . Therefore, with the conservation of mass, a phase transformation will lead to a change of volume which defines the transformation strain:

$$\epsilon_x^{tv} = \frac{1}{3} \epsilon_{x,vol}^{tv} \mathbf{I} = \frac{1}{3} \left(\frac{\rho_0}{\rho_x} - 1 \right) \mathbf{I} \quad (11)$$

The TRIP strain is caused by phase transformation under applied stress. The physics behind the mechanism is described in e.g. [43,44, 64]. In this paper, we allow for TRIP to occur during the diffusionless transformation of austenite into martensite by adopting the formulation proposed by [30, 32], with transformation stiffness parameters K_{tp} acquired by [35]. With our methodology of modeling each phase individually, the TRIP strain ϵ^{tp} is implemented in the individual material models of both martensite and austenite to generate the correct TRIP strain output after homogenization, see discussion in Section 5.4. In the martensite constitutive model, ϵ^{tp} is implemented as follows:

$$\dot{\epsilon}_m^{tp} = \frac{3}{2} K_{tp} \sigma_{m,dev} \frac{df(p_m)}{dp_m} \dot{p}_m \quad (12)$$

with

$$K_{tp}(\sigma_{m,e}) = K_{tp1} + K_{tp2} \sigma_{m,e} \quad (13)$$

For better numerical stability when the constitutive model is implemented and used in an FE-solver, we introduce an adaptation of the saturation function $f(p_m)$, still satisfying $f(0) = 0$ and $f(1) = 1$:

$$f(p_m) = p_m^2 \quad \Rightarrow \quad \frac{df(p_m)}{dp_m} = 2p_m \quad (14)$$

Together with the continuous evolution of martensite volume fraction during initial martensite nucleation ($p_m \ll 1$) this adaptation allows for a gentle start of the TRIP strain evolution. In these expressions we have introduced the (volume) phase fraction of martensite p_m and the equivalent von Mises stress $\sigma_{m,e} = \sqrt{3/2} \sigma_{m,dev} : \sigma_{m,dev} = \sqrt{3/2} |\sigma_{m,dev}|$.

Similarly, for TRIP strain implementation in the austenite constitutive model the expression takes the following form:

$$\dot{\epsilon}_a^{tp} = 3K_{tp} \sigma_{a,dev} p_m \dot{p}_m \quad (15)$$

Note that the expression uses the martensite volume fraction evolution \dot{p}_m . This prevents TRIP strains to develop during austenitization.

3.3. Plasticity and hardening model

We adopt the Chaboche plasticity model proposed in e.g. [65] that includes the von Mises yield function, non-linear isotropic and kinematic hardening. The von Mises type yield surface is here defined as:

$$\Phi_x = \sqrt{\frac{3}{2}} |\sigma_{x,dev} - \mathbf{X}_x| - (R_x + \sigma_{x,Y}) \quad (16)$$

where \mathbf{X}_x is the kinematic hardening stress (back-stress), R_x is the isotropic hardening stress (drag-stress) and $\sigma_{x,Y}$ is the initial yield stress. This yield function is used to distinguish elastic and plastic response via the conditions:

$$\Phi_x \leq 0, \quad \dot{\lambda}_x \geq 0, \quad \dot{\lambda}_x \Phi_x = 0 \quad (17)$$

where $\dot{\lambda}_x$ is the plastic multiplier. It is when $\dot{\lambda}_x > 0$ (and $\Phi_x = 0$) that plastic strain and hardening variables evolve. The evolution equation for the plastic strain is assumed to be of associate type:

$$\dot{\epsilon}_{x,p}^p = \dot{\lambda}_x \frac{\partial \Phi_x}{\partial \sigma_x} = \dot{\lambda}_x \sqrt{\frac{3}{2}} \frac{\sigma_{x,dev} - \mathbf{X}_x}{|\sigma_{x,dev} - \mathbf{X}_x|} \quad (18)$$

The total kinematic hardening stress \mathbf{X}_x is obtained from adding n_x kinematic hardening stresses $\mathbf{X}_{x,i}$ each following [66] type of evolution law:

$$\dot{\mathbf{X}}_x = \sum_{i=1}^{n_x} \dot{\mathbf{X}}_{x,i} = \sum_{i=1}^{n_x} \dot{\lambda}_x \left(\sqrt{\frac{3}{2}} C_{x,i} \frac{\sigma_{x,dev} - \mathbf{X}_x}{|\sigma_{x,dev} - \mathbf{X}_x|} - \gamma_{x,i} \mathbf{X}_{x,i} \right) \quad (19)$$

Finally, the evolution of isotropic hardening is adopted as follows:

$$\dot{R}_x = \dot{\lambda}_x b_x (R_{x,\infty} - R_x) \quad (20)$$

The material parameter values are assumed to be temperature dependent. We adopt the choices of these for all the phases from [26].

3.4. Numerical implementations

We apply the implicit backward Euler time integration scheme to the constitutive equations and follow the procedure to solve the arising nonlinear equations as outlined in e.g. [67]. The assumptions are that a time increment Δt from time ${}^n t$ to ${}^{n+1} t$, the strain increment $\Delta \epsilon_x$ and the temperature increment ΔT are given. Thereby also the change of the volume fractions p_x are given. In addition, the internal variables $\mathbf{X}_{x,i}$, R_x , $\epsilon^{x,p}$ and stress σ_x are assumed to be given at the previous time step ${}^n t$. Output from the procedure (the constitutive driver) is internal variables and stress for time ${}^{n+1} t$ as well as algorithmic tangent stiffness $\mathbf{E}_x = d\sigma_x/d\epsilon_x$. We can note that

for the case of martensite $x = m$, the TRIP strain will cause Hooke's law to become a nonlinear equation in the deviatoric stress also for an elastic response.

4. Homogenization methods

4.1. Preliminaries

Four homogenization methods will be adopted: isostrain (Voigt), isostress (Reuss), self-consistent and the Linear mixture rule. For all methods we assume that the temperature T is the same in all the phases. Results from the first three will be compared against that from the last since that is most commonly used. Further, the methods are implemented by using an incremental strain-driven algorithm. The state from the previous timestep ${}^n t$ is assumed to be given in terms of homogenized strain ${}^n \bar{\epsilon}$ and stress ${}^n \bar{\sigma}$ as well as strain ${}^n \epsilon_x$, stress ${}^n \sigma_x$ and state variables for all the phases. Then a strain increment $d\bar{\epsilon}$ is applied whereby the updated homogenized strain can be computed as $\bar{\epsilon} = {}^n \bar{\epsilon} + d\bar{\epsilon}$ but the increments $d\bar{\sigma}$, $d\epsilon_x$ and stress $d\sigma_x$ are determined by the chosen homogenization method.

During a time increment of the mechanical problem it is assumed that the temperature and phase fractions remain constant. Hence, the relation between the homogenized strain increment and strain increment of the phases can be written as:

$$d\bar{\epsilon} = \sum_{x=1}^{n_x} p_x d\epsilon_x \quad (21)$$

and similarly between the stress increments

$$d\bar{\sigma} = \sum_{x=1}^{n_x} p_x d\sigma_x \quad (22)$$

In addition, the strains ϵ_x^{th} and ϵ_x^{tv} and their increment $d\epsilon_x^{\text{th}}$ and $d\epsilon_x^{\text{tv}}$ are given as the temperatures at the start and end of the current time increment is known. For convenience, we introduce the strain variable $\epsilon_x^{\text{t}} = \epsilon_x^{\text{th}} + \epsilon_x^{\text{tv}}$ and its increment $d\epsilon_x^{\text{t}}$, which are also known.

4.2. Isostrain - Voigt assumption

For the isostrain (Voigt) assumption the strain increment of all the phases $d\epsilon_x$ are assumed to be equal to the homogenized strain increment, i.e. $d\epsilon_x = d\bar{\epsilon}$. Therefore, the homogenized stress increment can be obtained as follows:

$$d\bar{\sigma} = \sum_{x=1}^{n_x} p_x \mathbf{E}_x : (d\epsilon_x - d\epsilon_x^{\text{t}}) = \sum_{x=1}^{n_x} p_x \mathbf{E}_x : (d\bar{\epsilon} - d\epsilon_x^{\text{t}}) \quad (23)$$

where \mathbf{E}_x is the consistent algorithmic tangent stiffness. By comparing to a homogenized model $d\bar{\sigma} = \bar{\mathbf{E}} : (d\bar{\epsilon} - d\bar{\epsilon}^{\text{t}})$ we can obtain the homogenized tangent stiffness

$$\bar{\mathbf{E}} = \frac{d\bar{\sigma}}{d\bar{\epsilon}} = \sum_{x=1}^{n_x} p_x \frac{d\sigma_x}{d\bar{\epsilon}} = \sum_{x=1}^{n_x} p_x \frac{d\sigma_x}{d\epsilon_x} = \sum_{x=1}^{n_x} p_x \mathbf{E}_x \quad (24)$$

and the homogenized strain

$$d\bar{\epsilon}^{\text{t}} = \bar{\mathbf{E}}^{-1} : \sum_{x=1}^{n_x} p_x \mathbf{E}_x : d\epsilon_x^{\text{t}}$$

where $d\bar{\epsilon}^{\text{t}} = d\bar{\epsilon}^{\text{th}} + d\bar{\epsilon}^{\text{tv}}$.

4.3. Isostress - Reuss assumption

For the isostress (Reuss) assumption the stress increment $d\sigma_x$ is assumed to be the same in all the phases and thereby equal to the homogenized stress, i.e. $d\sigma_x = d\bar{\sigma}$. The homogenized strain increment can be obtained as

$$d\bar{\epsilon} = \sum_{x=1}^{n_x} p_x d\epsilon_x = \sum_{x=1}^{n_x} p_x (\mathbf{E}_x^{-1} : d\sigma_x + d\epsilon_x^t) = \sum_{x=1}^{n_x} p_x (\mathbf{E}_x^{-1} : d\bar{\sigma} + d\epsilon_x^t) \quad (25)$$

By comparing to a homogenized model $d\bar{\epsilon} = \bar{\mathbf{E}}^{-1} : d\bar{\sigma} + d\bar{\epsilon}^t$ we obtain the homogenized stiffness

$$\bar{\mathbf{E}} = \left(\sum_x^n p_x \mathbf{E}_x^{-1} \right)^{-1}$$

and the homogenized thermal strain components

$$d\bar{\epsilon}^t = \sum_x^n p_x d\epsilon_x^t$$

However, since the model will be used together with FEM, our numerical implementation of the cyclic plasticity model is based on a strain controlled algorithm (given $d\bar{\epsilon}$). This means that we need an additional Newton iteration scheme to find each phase's individual strain increment, $d\bar{\epsilon} = [d\epsilon_1, \dots, d\epsilon_{n_x}]^T$, such that the isostress criteria is fulfilled. This procedure is presented in [Algorithm 1](#), the reader may notice the similarity to a 2 D plane stress algorithm.

Algorithm 1. Isostress - individual phase strain update

Initiate phase strain increments $d\bar{\epsilon} = [d\epsilon_1, \dots, d\epsilon_{n_x}]^T$

while $error < TOL$ **do**

 Compute individual phase stress increments $d\bar{\sigma}(d\bar{\epsilon}, T, t)$ (See [Section 3.4](#))

 Compute residual $\underline{\mathbf{R}}(d\bar{\epsilon}, d\bar{\sigma}) = [\mathbf{R}_{\bar{\epsilon}}, \mathbf{R}_x]^T$

$$\mathbf{R}_{\bar{\epsilon}} = \sum_{x=1}^{n_x} p_x d\epsilon_x - d\bar{\epsilon}$$

$$\mathbf{R}_x = d\sigma_x - d\sigma_{x+1} \quad \text{for } x = 1, \dots, (n_x - 1)$$

 Update individual phase strain increments $d\bar{\epsilon} = d\bar{\epsilon} - \left(\frac{d\mathbf{R}}{d\bar{\epsilon}} \right)^{-1} : \underline{\mathbf{R}}$

 Compute error $error = |\underline{\mathbf{R}}|$

end while

Compute individual phase strain derivative $\frac{d\bar{\epsilon}}{d\bar{\epsilon}} = \left[\frac{d\epsilon_1}{d\bar{\epsilon}}, \dots, \frac{d\epsilon_x}{d\bar{\epsilon}} \right] = - \left(\frac{\partial \mathbf{R}}{\partial \bar{\epsilon}} \right)^{-1} \circ \frac{\partial \mathbf{R}}{\partial \bar{\epsilon}}$

Compute tangent stiffness $\frac{d\bar{\sigma}}{d\bar{\epsilon}} = \sum_x^n p_x \frac{d\bar{\sigma}}{d\epsilon_x} : \frac{d\epsilon_x}{d\bar{\epsilon}}$

return $d\bar{\epsilon}, \frac{d\bar{\sigma}}{d\bar{\epsilon}}$

[Algorithm 1](#) uses the unbalance tensor Jacobian computed as:

$$\frac{\partial \mathbf{R}_{\bar{\epsilon}}}{\partial \epsilon_x} = p_x \mathbf{1}, \quad \frac{\partial \mathbf{R}_x}{\partial \epsilon_y} = \delta_{xy} \frac{\partial \sigma_x}{\partial \epsilon_y} - \delta_{(x+1)y} \frac{\partial \sigma_{x+1}}{\partial \epsilon_y} \quad \text{for } x = 1, \dots, (n_x - 1), \quad y = 1, \dots, n_x \quad (26)$$

where $d\epsilon_x/d\bar{\epsilon}$ is obtained from $\underline{\mathbf{R}}(d\epsilon_x; d\bar{\epsilon}) = \underline{\mathbf{0}}$ for all $d\bar{\epsilon}$.

4.4. Self-consistent homogenization

By adopting the self-consistent framework described in [68], the strain increment in each phase $d\epsilon_x$ can be expressed as:

$$d\epsilon_x = \mathbf{A}_x : d\bar{\epsilon} \quad (27)$$

with the fourth order concentration tensor \mathbf{A}_x defined as:

$$\mathbf{A}_x = (\mathbf{I} + \mathbf{P} : (\bar{\mathbf{E}}^{-1} : \mathbf{E}_x - \mathbf{I}))^{-1} \quad (28)$$

\mathbf{P} is the Eshelby tensor which is computed using the fixed-point iteration technique described in [69,70]. The homogenized stress increment can be obtained as follows:

$$d\bar{\sigma} = \sum_{x=1}^{n_x} p_x \mathbf{E}_x : (d\epsilon_x - d\epsilon_x^t) = \sum_{x=1}^{n_x} p_x \mathbf{E}_x : (\mathbf{A}_x : d\bar{\epsilon} - d\epsilon_x^t) \quad (29)$$

By comparing to a homogenized model $d\bar{\sigma} = \bar{\mathbf{E}} : (d\bar{\epsilon} - d\bar{\epsilon}^t)$ we can obtain the homogenized tangent stiffness

$$\bar{\mathbf{E}} = \frac{d\bar{\sigma}}{d\bar{\epsilon}} = \sum_{x=1}^{n_x} p_x \frac{d\sigma_x}{d\bar{\epsilon}} = \sum_{x=1}^{n_x} p_x \frac{d\sigma_x}{d\epsilon_x} : \mathbf{A}_x = \sum_{x=1}^{n_x} p_x \mathbf{E}_x : \mathbf{A}_x \quad (30)$$

and the homogenized strain

$$\begin{aligned} d\bar{\epsilon}^t &= d\bar{\epsilon} - \bar{\mathbf{E}}^{-1} : d\bar{\sigma} = d\bar{\epsilon} - \bar{\mathbf{E}}^{-1} : \sum_{x=1}^{n_x} p_x \mathbf{E}_x : (\mathbf{A}_x : d\bar{\epsilon} - d\epsilon_x^t) \\ &= \left(\mathbf{I} - \bar{\mathbf{E}}^{-1} : \sum_{x=1}^{n_x} p_x \mathbf{E}_x : \mathbf{A}_x \right) : d\bar{\epsilon} + \bar{\mathbf{E}}^{-1} : \sum_{x=1}^{n_x} p_x \mathbf{E}_x : \mathbf{A}_x : d\epsilon_x^t \end{aligned} \quad (31)$$

The adopted fixed point iteration procedure to determine \mathbf{A}_x is described in [Algorithm 2](#). This is used as a pre-processing step at the start of each time step to determine the strain increment of each constitutive phase.

Algorithm 2. Self-consistent - Concentration tensor fixed-point iteration

```

Load previous time step global tangent stiffness tensor  ${}^{k=0}\bar{\mathbf{E}} = {}^n\bar{\mathbf{E}}$ 
Load previous time step phase tangent stiffness tensors  ${}^n\mathbf{E}_x$ 
while error < TOL do
    Iteration  $k = k + 1$ 
    Compute Eshelby tensor  ${}^{(k)}\mathbf{P} = \mathbf{P}({}^{(k-1)}\bar{\mathbf{E}})$  (see [69])
    Compute concentration tensors  ${}^{(k)}\mathbf{A}_x = (\mathbf{I} + {}^{(k)}\mathbf{P} : ({}^{(k)}\bar{\mathbf{E}}^{-1} : {}^n\mathbf{E}_x - \mathbf{I}))^{-1}$ 
    Update stiffness tensor  ${}^{(k)}\bar{\mathbf{E}} = \sum_{x=1}^{n_x} p_x {}^n\mathbf{E}_x : {}^{(k)}\mathbf{A}_x : (\sum_{x=1}^{n_x} p_x {}^{(k)}\mathbf{A}_x)^{-1}$ 
    Compute error =  $|{}^{(k)}\bar{\mathbf{E}} - {}^{(k-1)}\bar{\mathbf{E}}|$ 
return Concentration tensors  $\mathbf{A}_x$ 
    
```

4.5. Linear mixture rule

The linear mixture rule is the most used and most straight forward way of handling multi-phase states in steel, see e.g. [23] and [32]. Therefore, we include this as a point of reference when comparing the isostrain, isostress, and self consistent homogenization methods. When using the linear mixture rule the constitutive phases are not treated by individual material models, but as one nominal model where all thermal and mechanical properties are computed as the volume fraction

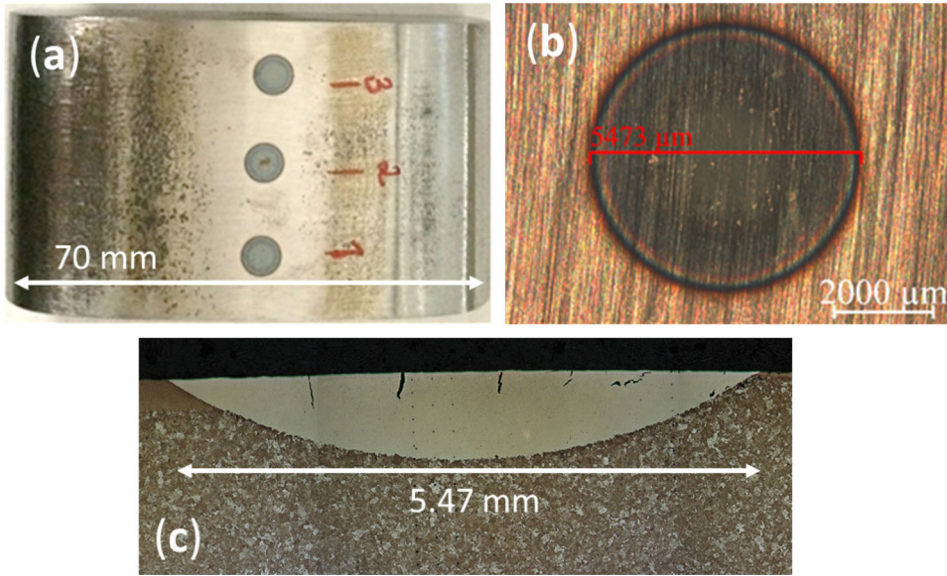


Figure 2. Experimental WEL on rail surface, from [58, 72]. (a) rail used in i experiment, (b) close up of laser heated WEL spot, and (c) cross sectional view of WEL.

governed average of phases present, exemplified in Equation 32 for the fourth order elasticity tensor \mathbf{E}^e .

$$\mathbf{E}^e = \sum_{x=1}^{n_x} p_x \mathbf{E}_x^e \quad (32)$$

5. Thermo-mechanical simulation of laser pulse induced white etching layer

The constitutive models presented in Section 3 and the homogenization methods in Section 4 are implemented as user defined subroutines in Abaqus [71]. These are used in thermo-mechanical FE-simulations of a laser heating experiment performed in [58, 72]. Experimental results are phase transformations and residual stresses which are compared against simulation results. In particular, the influence of including the TRIP-effect in the modeling, the choice of homogenization method and effect of cyclic thermal straining are investigated.

5.1. Laser heating experiment and residual stress measurements

In the laser heating experiment [58, 72], martensitic spots, so called white etching layers (WEL), are induced on the surface of pearlitic R260 rail steel by laser heating a small spot above austenitization temperature for 1 second. As the heat-pulse is short, the surrounding material is still close to room temperature, whereby heat diffusion causes rapid cooling and effectively quenches the austenite to form a thin disk of martensite. Stereo and optical microscopy are used to characterize the microstructural changes, and residual stress measurements are performed using X-ray diffraction. Figure 2 presents the laser heated spots, as well as the microstructural change of the WEL.

5.2. Description of FE-model and simulation

The FE simulations use a one-way thermo-mechanical coupling; results from a transient heat transfer simulation drive the phase transformations and mechanical response in the subsequent

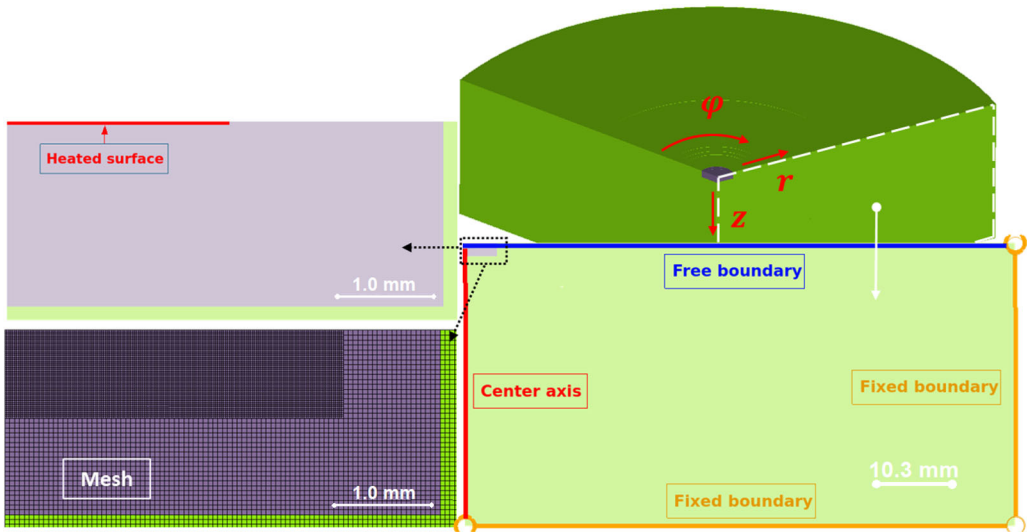


Figure 3. Axisymmetric FE model with cylindrical coordinate system $r - \varphi - z$, presenting boundary conditions, close up of area with refined mesh, and the heated part of the surface.

structural simulations. This setup means that thermal aspects of plasticity induced dissipative heat and latent heat are not accounted for. Both transient heat and structural simulations use the same axisymmetric model, see Figure 3. The constitutive models of Section 3 are used close to the heated surface (purple region in Figure 3). The surrounding region (green in figure) uses a linear elastic material model (Young's modulus $E = 210 \text{ GPa}$ and Poisson's ratio $\nu = 0.3$) as, in this far-field region, stresses do not reach the pearlitic steel initial yield limit and temperatures stay below the austenitization temperature.

Figure 3 shows how the area of interest, where the heat is applied and the martensitic disk will form, is meshed using a very fine resolution and how the mesh gets stepwise coarser further away. The thermal and mechanical simulations use the same mesh where the representative element length of the fine resolution is approximately 0.02 mm. The purple region is discretized using fully integrated second order quadratic elements and the green far-field single-phase region using first order elements. The figure shows the fixed boundary conditions of the internal rail boundaries and the free surface at the top of the rail. For the heat transfer simulation, convective boundary condition is implemented for the rail surface, as proposed in [73], while the internal boundary conditions are modeled as perfectly insulated. We deem the effect of the choice of internal boundary conditions as negligible since the width of the FE-model is about 35 times that of the heated surface. Heat is uniformly applied for 1 s, after which the structure is left to cool for 100 s.

In this paper we adopt the temperature dependent model parameter values for the phases presented in [26]. TRIP strain related material parameters are obtained from [35] and are not temperature dependent. The temperature dependent values were found by calibration against a combination of cyclic experimental data and data predicted by the software JMatPro [74]. It should be noted that the data used in [26] is for the pearlitic wheel steel ER7 [75], whereas the experiment is performed using pearlitic rail steel R260 [59]. The wheel steel has a finer pearlite lamellar spacing due to forced cooling in production while the rail steel has slightly higher carbon content and thus higher pearlite phase fraction. This results in similar strength and cyclic plastic behavior at room temperature. Since cyclic data at elevated temperatures is not yet available to us for R260, we assume that the high temperature behavior is the same given the similarity in chemical composition and microstructure. Also the main focus of this paper is evaluating and comparing the effect of three proposed homogenization methods rather than material model calibration.

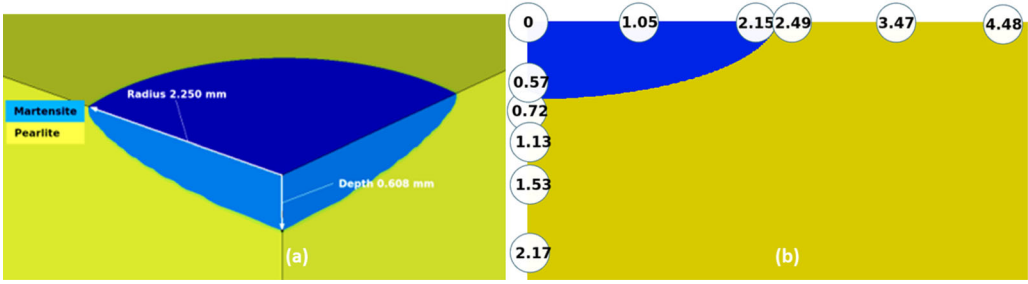


Figure 4. (a) Martensitic disk (WEL) obtained in the FE-simulation of the laser heating experiment. (b) definition of data points (in the radial direction r and in the depth direction z as defined Figure 3) used for presentation of results.

Furthermore, the heat load in the simulations is tuned such that the obtained WEL is of the same size as that presented in Figure 2. Only the heat flux magnitude is tuned as the duration of the experimental heat pulse is known. The magnitude of the heat flux is tuned to 50 W/m^2 with a cutoff temperature of 1200°C , noting that this cutoff temperature is higher than what is used in many weld simulations [3]. Also, available knowledge of mechanical behavior is scarce in this temperature range.

5.3. Simulation of temperature driven phase transformations

This section presents the metallurgical response of the transient heat driven structural simulation described in the previous section. The simulation shows how a martensitic disk is formed, see Figure 4, which after tuning the heat flux correlates in both size and shape with that seen in the experimental results in Figure 2. The cooling stage of the simulation is presented in Figure 5, where the temperature histories in the data points of the disk (defined in Figure 4b) are plotted in relation to the IT-diagram used in the transformation kinetics model for illustrational purposes only; the computations are (as defined above) step-wise isothermal using the additive assumption.

The strong temperature transients in the central locations are clearly seen. In all points where the temperature has reached above the austenitization temperature the cooling is fast and a fully martensitic structure is formed. Furthermore, by observing that the points in Figure 4(b) are closely located it is clear that also the spatial temperature gradient is very high. This motivates why a very fine mesh must be used in the FE simulations.

5.4. Simulation results motivating the importance of including the TRIP-effect

To study how results are affected by the TRIP-effect, we simulate an unconstrained thermal dilatation experiment with and without TRIP included. Figure 6 shows a single Gauss-point dilatation simulation where the pearlitic steel is heated from 20°C to 1000°C in 1 s and then cooled back to 20°C in 1 s. The top graph shows the applied temperature and the resulting uniaxial strains, and the lower graph shows the phase transformations during both heating and cooling. To illustrate the influence of the TRIP-effect, different uniaxial stress conditions are applied just before the martensitic transformation starts. The results show how the residual strain is significantly altered from the yellow, stress-free curve by the contribution of ϵ^{tp} which according to (12) increases in the presence of deviatoric stress σ_{dev} . These results are for the isostrain homogenization method.

With our methodology of parallel constitutive models for all phases there is no inherent TRIP-effect. The $\epsilon_{\text{NoTRIP}, 100\text{MPa}}$ curve in Figure 6 shows that with the TRIP strain ϵ^{tp} excluded the straining from the 100 MPa axial load remains constant during the martensitic phase transformation, i.e. no additional strain is accumulated.

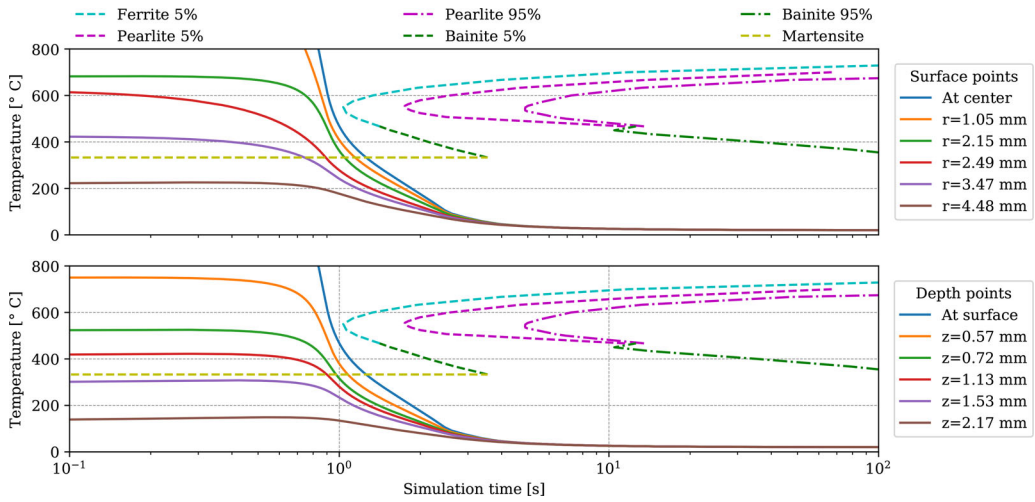


Figure 5. Temperature histories during the cooling in specific locations (defined in Figure 4(b)) shown together with the IT diagram of the material.

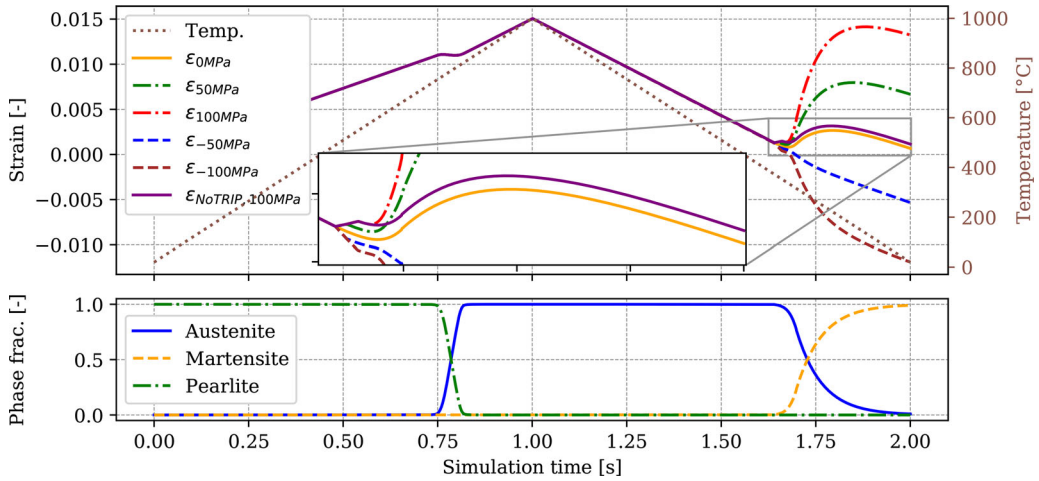


Figure 6. One Gauss-point dilatation simulation under uniaxial stress, isostrain homogenization.

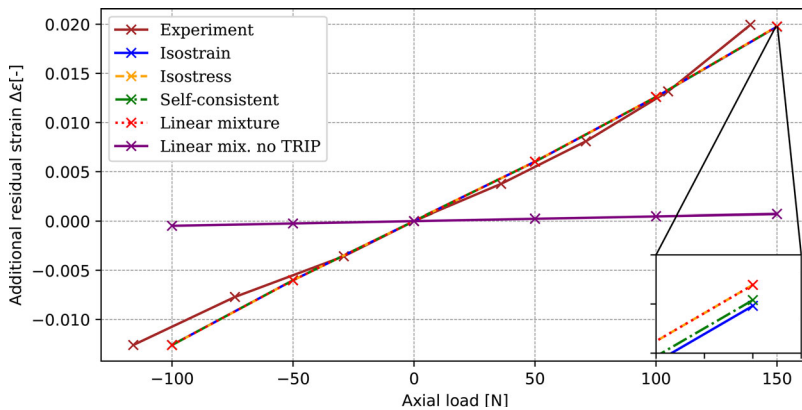


Figure 7. Residual strain from dilatation under uniaxial stresses. Experimental results [35] compared against single eight node element FE-simulation, isostrain, isostress, self consistent and linear mixture homogenization.

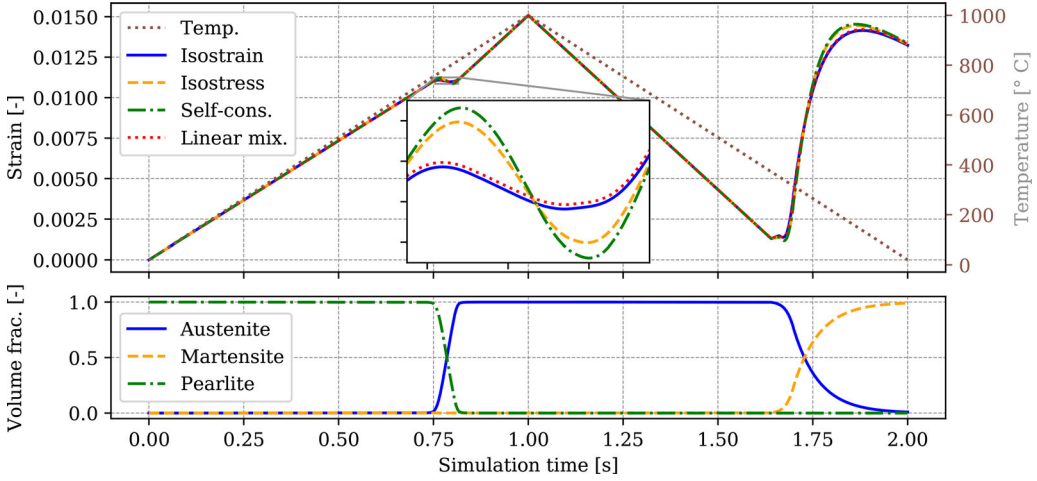


Figure 8. One Gauss-point dilatation simulation using different homogenization methods. The top graph presents temperature load and resulting dilatation strain under 100 MPa axial load, the bottom graph presents phase volume fractions.

To validate the implementation of the TRIP-effect, Equations (12)-(15), the additional residual strain from the axial load at the end of the thermal load cycle is compared to experimental results presented by Mahnken [35]. The simulated thermal load cycle and axial loads are adjusted to match that used in the experiment. Figure 7 presents the additional residual strain $\Delta\epsilon$ obtained using the different homogenization methods presented in Section 4.

Based on the results presented in Figure 7 the simulation results correlate reasonably well to experimental data. Whereby the TRIP-strain related parameters obtained from [35] are not adjusted in our implementation, although these are for a different steel grade. The figure also presents the additional residual strain obtained when excluding the TRIP strain ϵ_x^{tp} presented in Section 3.2, again highlighting the importance of incorporating the TRIP effect in the material modeling.

5.5. Simulation results illustrating the effects for different homogenization methods

In this section we compare FE-simulation results obtained using the different homogenization methods presented in Section 4.1, all including the TRIP-effect in the constitutive modeling of the austenite and martensite phases. First, the single Gauss-point dilatation simulation presented in Section 5.4 is used to illustrate local effects of the different homogenization methods. Figure 8 presents the temperature load, the resulting dilatation strain, and the phase volume fractions. Depending on the homogenization method used, the stages where more than one phase exist show a slight shift of the resulting strain. In stages where only one phase exists, as expected, all methods give identical results.

Next, we compare results of the laser heating experiment FE-simulation obtained using different homogenization methods. With individual phase constitutive models, the different homogenization methods result in different strain and internal variable histories for the phases, due to the discrepancies highlighted in Figure 8, and thereby different residual stress fields. This is illustrated in Figure 9, where the residual radial stress fields of the isostrain, isostress and self-consistent methods are presented, as well as that obtained using the linear mixture rule. It is noted that the all homogenization methods give compressive stress in the martensite and tensile stress in the surrounding pearlite, however the magnitudes of the stresses differ depending on homogenization method.

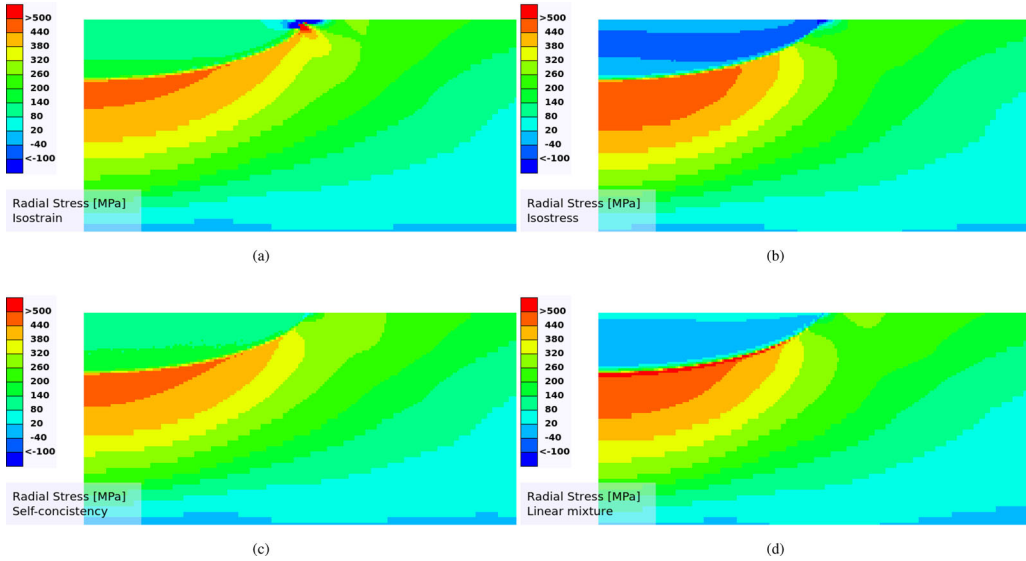


Figure 9. Residual radial stress simulation results, σ_r , for homogenization method (a) isostrain, (b) isostress and (c) self-consistent (d) linear mixture.

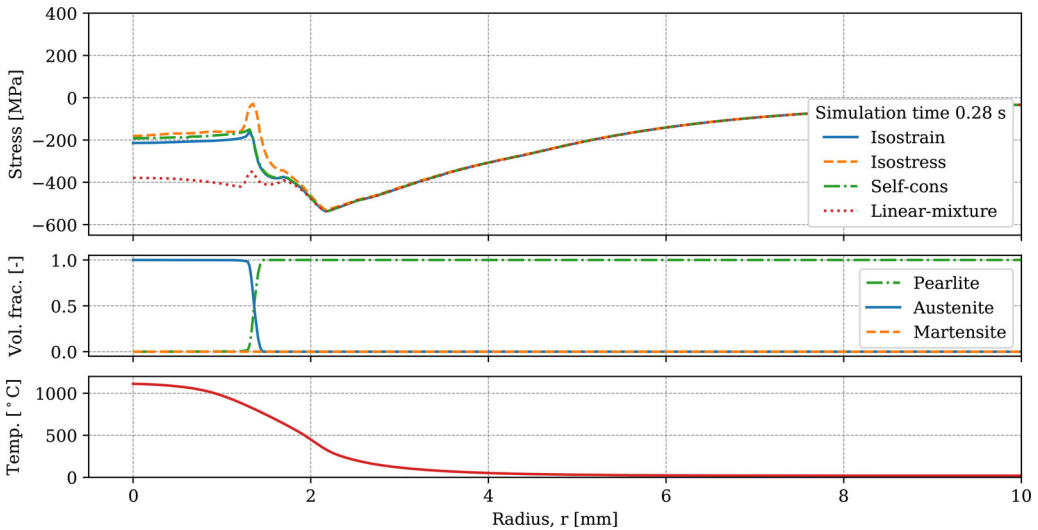


Figure 10. Radial stress, volume fraction and temperature at the surface of the FE-model at 0.28 s into the heating stage of the simulation.

To understand the residual stress differences, we study the stress evolutions during the laser heating simulations in further detail. Radial stress, phase volume fractions, and temperature on the heated rail surface are examined at different times during the heating and cooling stages of the simulation by plotting the results along the surface, i.e. along r (distance from the axisymmetry axis) at $z=0$ mm. In Figure 10 the results at 0.28 s into the heating stage of the simulation are shown. Here we see how austenite starts to form and how the thermal expansion of the heated region causes compressive stresses in the far-field region. As the volume of the nucleated austenite is smaller than that of its parent pearlite phase, see Figures 6 and 8, the compressive stresses decrease. The figure also shows how the homogenization methods produce significantly different stress magnitudes within the two-phase region and how part of these differences remains

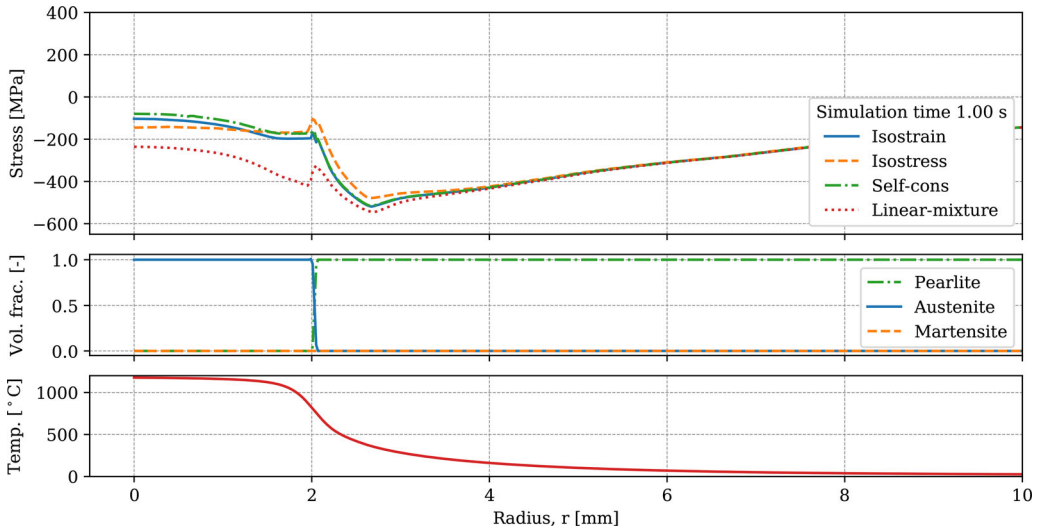


Figure 11. Radial stress, volume fraction and temperature at the surface of the FE-model at 1.0 s into the heating stage of the simulation.

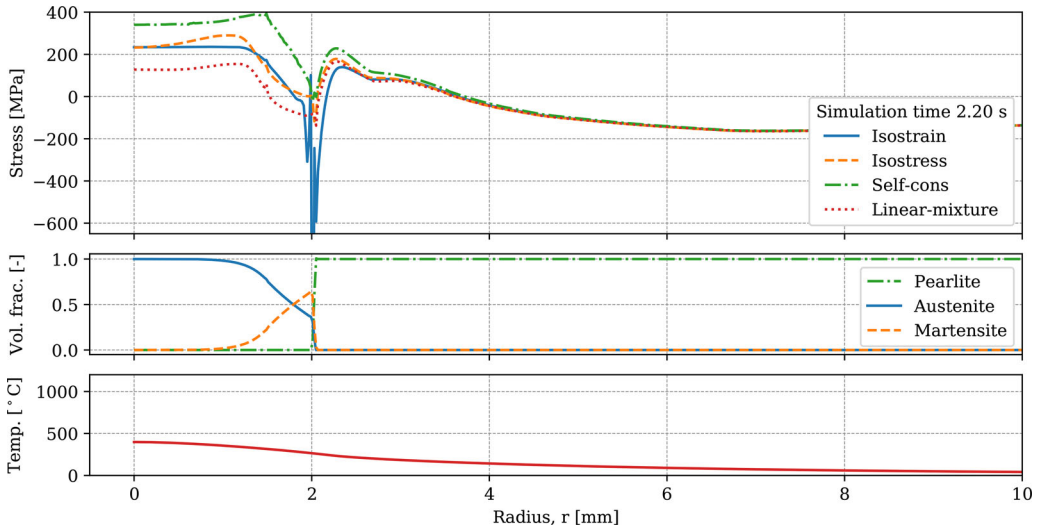


Figure 12. Radial stress, volume fraction and temperature at the surface of the FE-model at 2.20 s into the heating stage of the simulation.

once the transformation is complete. The isostress method produces large strains in the softer phase, thus causing more hardening of the softer austenite.

Figure 11 shows the state of the simulation at 1.0 s. Now the austenite disk is fully formed and the heat source is removed. Again, the effect of the homogenization methods' different strain histories is seen.

After 1.20 s into the cooling stage, the rapid temperature drop has quenched the austenite and martensite has formed, see Figure 12. Again, the isostrain assumption and the self-consistent scheme gives similar results, whereas the linear mixture assumption gives higher compressive stresses.

Figure 13 presents the residual stress state when the temperature is back at 20 ° C and the martensitic disk is fully formed. The figure also presents the experimental results of the residual

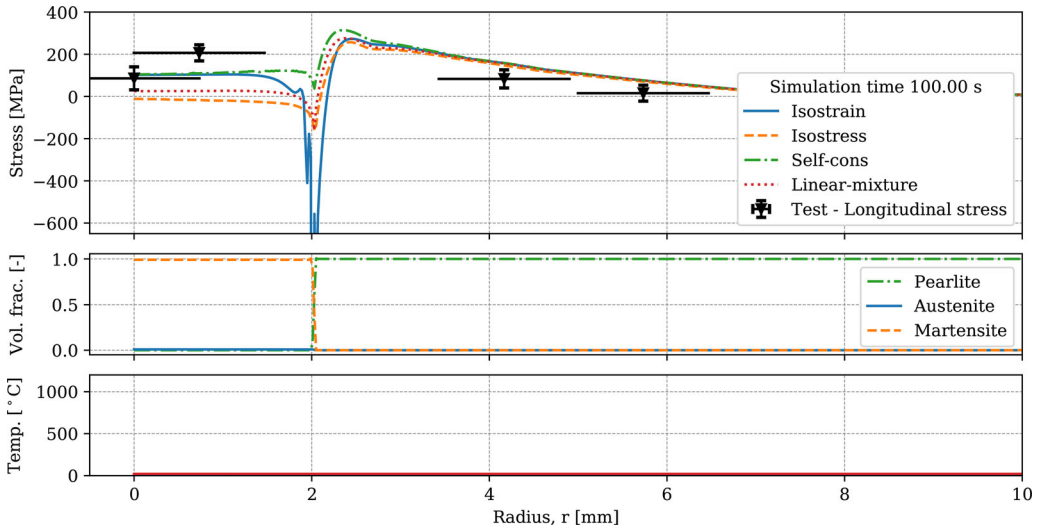


Figure 13. Residual stress, volume fraction and temperature at the surface of the FE-model at 100.0 s after the laser heating.

stresses described in Section 5.4. Comparing these to the results of the simulations, we see that none of the models give a perfect fit. However, despite the steel grade differing and the low level of load case parameter calibration, the trend is still captured and results are of the same order of magnitude.

By studying the series of graphs presented in Figures 10–13 we observe how the austenite starts forming at $r=0$ mm of the heated surface, see Figure 3, and grows outwards (and downwards) into the surrounding material. The cooling is driven by heat conduction to the surrounding material, hence the quenching transformation starts at the periphery of the austenitic disk and the transformation front moves toward the center (and surface) of the WEL-disk. These sequential transformations and the thermal expansion causes cyclic straining, explained in detail by Şimşir et al. [76]. Due to this pendulum transformation front from heating and cooling, the choice of homogenization method has a pronounced effect on stress and strain field as well as evolution of internal variables in the phases. This difference in internal variable histories for the different homogenization methods is a result of the discrepancies highlighted in Figure 8 and it explains the residual states presented in Figure 9.

To illustrate the effect of this cyclic loading for different homogenization methods we focus on the austenitic phase and study its accumulation of the plastic strain multiplier λ at measuring point 0 in Figure 4. The result during the first 3 s of the simulation is shown in Figure 14, together with phase volume fractions and temperature. Here we see that when using the isostress method, enforcing the stress of the parent pearlite onto the nucleated austenite causes more plastic material response than when enforcing the parent strain using the isostrain method. Using the self-consistent scheme, the plastic response is very similar to that of the isostrain method. The graphs also exemplifies our multi-phase simulation methodology where as mentioned in Section 4, the response of each phase is computed at every time step but the phase is only allowed to accumulate hardening once its volume fraction is greater than zero. This is seen by how the austenite plastic strain multiplier curve starts to grow only once the austenite volume fraction is greater than zero. The graph also shows how the plastic strain multiplier remains constant after that the austenite volume fraction becomes zero.

By comparing the results from the homogenization methods we can observe how the short multi-phase stages of the simulations govern the outcome. If other load cases were simulated, the multi-phase stages would appear for different durations, at different stress states, and possibly in different sequence. A corresponding comparison of the homogenization methods would then give

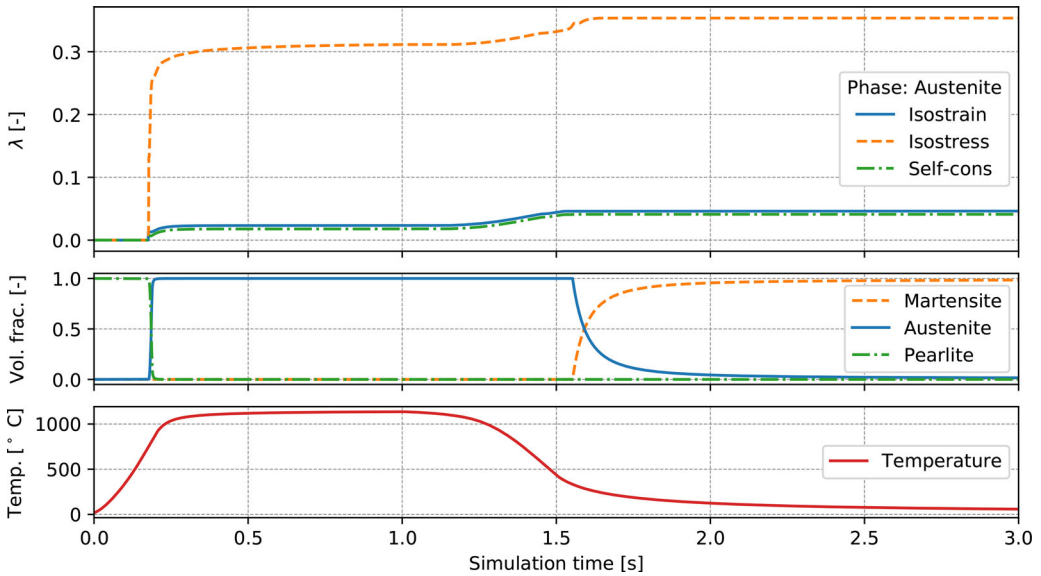


Figure 14. Accumulated plastic multiplier λ for the three studied homogenization methods, phase fraction evolution, and temperature at the WEL disk surface center.

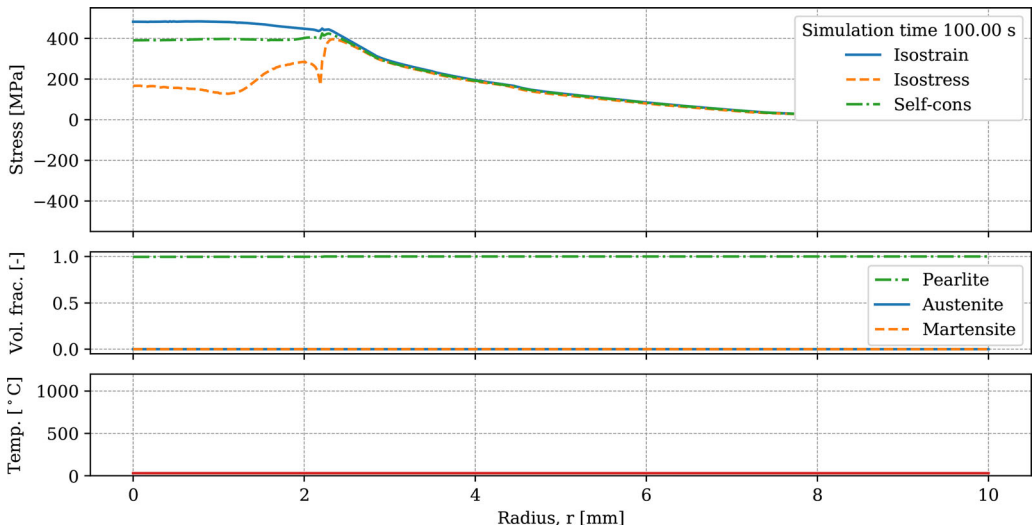


Figure 15. Radial stress, volume fraction and temperature at the surface of the FE-model at 100.0s into the *slow* cooling simulation.

a different outcome. We obtain this when re-running the simulation but with the heat source removed gradually. This generates lower cooling rates whereby pearlite is forming instead of martensite. Figure 15 shows the results from the slower cooling rate simulation, presenting the residual surface stresses, phase volume fractions, and temperature on the surface ($z = 0$ mm) for the different homogenization methods. The difference in plastic strain evolution during the austenitization, seen in Figure 14, and also during the reforming of pearlite now causes a more pronounced difference in the residual stress state also between the isostrain and the self-consistent method. The underlying reason is that pearlite is softer than martensite and do not include any TRIP-strain.

Table 1. Computational time (wall-clock-time) for each homogenization method simulation.

	isostrain	isostress	self consistent	single-phase
Comput. time	4h 18 min	9h 42 min	4h 20 min	56 min

6. Conclusions and outlook

This paper is an extension of the material model framework for phase transformations and cyclic plasticity of pearlitic steels presented in our previous work [26]. The framework is extended by investigating different homogenization methods, including the TRIP-effect, and also by more physically realistic internal variable inheritance. We can conclude from the results that it is important to include the TRIP-effect when modeling martensite formation in pearlitic steels. In this paper we propose a modification of the saturation function from [35], see Equation 14, which gives a smoother evolution of the TRIP strain while retaining the total magnitude after complete transformation. This modification improves the numerical stability of the material model which is important when implemented in an FE-solver.

Besides the isostrain homogenization method, the isostress and the self-consistent methods are also investigated. The main purpose is to study the influence of the homogenization method in applications of heating and cooling with resulting phase transformations of pearlitic steels. In this context, numerical algorithms for implementing these homogenization methods are described. Based on these and the results of the simulations we conclude that the additional Newton iteration scheme required by the isostress method causes longer computational time and greater risk for numerical instabilities as compared to the isostrain method. The reason for numerical instabilities is that there is a significant difference in stress-strain response of the different phases at high temperatures. Therefore, extreme strains can be produced when the stress state of the parent phase is imposed onto the nucleated phase. The adopted algorithm (from [68]) of the self-consistent method does not have this instability issue. However, it does demand a pre-processing step to compute the concentration tensors and therefore requires more computational time than the isostrain method, but less than the isostress method. The computational time for each homogenization method simulation is presented in Table 1. For comparison, the table also presents the computational time of a simulation where phase transformations are not included, i.e. heating and cooling of single-phase pearlitic steel modeled using the von Mises plasticity model described in Section 3.3. The computational time increases significantly using homogenization methods compared to neglecting the phase transformations using a single phase model. The isostrain method increase the computational time with a factor of roughly 4.7 and the isostress method a factor of 10 due to the additional algorithm, see Algorithm 1 in Section 4.3. The computations were performed on a computer cluster using 32 cores (Intel Xeon Gold 6230) and 384 GB RAM.

From the simulation results for the different homogenization methods we conclude that it is the short multi-phase stages that generate the difference between the methods. Especially the evolution of plasticity is affected, which results in different residual stress and strain states. In the example of the laser heating, the isostrain and the self-consistent method differ the least after the final cooling stage. The results from these methods indicate a better agreement with experimental results as compared to results from the isostress method. We should emphasize that the available experimental data is limited and therefore strong conclusions cannot be made.

The homogenization algorithms were also compared for the case when the rapid cooling in the laser heating experiments was replaced by slower cooling. For this case austenite was transformed back into pearlite instead of martensite. The results showed a more significant difference between the isostrain and the self-consistent method. The residual stress computed with the self-consistent method was in between the results from the isostrain and the isostress method. This indicates that the self-consistent method is more accurate than the extreme cases of isostrain and isostress. This is also in agreement with results in literature for other materials see e.g. [57].

Together with the relatively good computational efficiency of the self-consistent method, we would like to indicate that it is the most promising of the investigated homogenization methods for the investigated application. However, further experimental studies and comparison against these are needed before a strong conclusion can be made.

Note

1. In a Cartesian coordinate system the components of the second order identity tensor is given by the Kronecker's delta δ_{ij} , i.e. $I_{ij} = \delta_{ij}$. The components of \mathbf{I} are given as $I_{ijkl} = \delta_{ik}\delta_{jl}$. The open product defined as $(\mathbf{A} \otimes \mathbf{B})_{ijkl} = A_{ij}B_{kl}$. Double contraction between a fourth and second order tensor $(\mathbf{A} : \mathbf{B})_{ij} = A_{ijkl}B_{kl}$.

Acknowledgments

The current study is part of the ongoing activities in CHARMEC – Chalmers Railway Mechanics (www.chalmers.se/charmec). The numerical simulations were performed on resources provided by Chalmers e-Commons (C3SE).




Disclosure statement

No potential conflict of interest was reported by the authors.

Funding

Parts of the study have been funded from the European Union's Horizon 2020 research and innovation programme in the projects In2Track2 and In2Track3 under grant agreements Nos 826255 and 101012456.

ORCID

Johan Ahlström  <http://orcid.org/0000-0002-2672-4547>
 Magnus Ekh  <http://orcid.org/0000-0001-6925-7806>
 B. Lennart Josefson  <http://orcid.org/0000-0003-1202-3624>

References

- [1] E. Pereloma and D. Edmonds, *Phase Transformations in Steel*. Cambridge: Woodhead Publishing Limited, 2012.
- [2] L. E. Lindgren, "Finite element modeling and simulation of welding part 1: Increased complexity," *J. Thermal Stresses*, vol. 24, no. 2, pp. 141–192, 2001. DOI: [10.1080/01495730150500442](https://doi.org/10.1080/01495730150500442).
- [3] L.-e. Lindgren, "Finite element modeling and simulation of welding Part 2: Improved material modeling," *J. Thermal Stresses*, vol. 24, no. 3, pp. 195–231, 2001. DOI: [10.1080/014957301300006380](https://doi.org/10.1080/014957301300006380).
- [4] L. E. Lindgren, "Finite element modeling and simulation of welding Part 3: Efficiency and integration," *J. Thermal Stresses*, vol. 24, no. 4, pp. 305–334, 2001. DOI: [10.1080/01495730151078117](https://doi.org/10.1080/01495730151078117).
- [5] F. Rammerstorfer, D. Fischer, W. Mitter, K. Bathe and M. Snyder, "On thermo-elastic-plastic analysis of heat-treatment processes including creep and phase changes," *Comput. Struct.*, vol. 13, no. 5–6, pp. 771–779, 1981. DOI: [10.1016/0045-7949\(81\)90040-7](https://doi.org/10.1016/0045-7949(81)90040-7).
- [6] F. M. B. Fernandes, S. Denis and A. Simon, "Mathematical model coupling phase transformation and temperature evolution during quenching of steels," *Mater. Sci. Technol.*, vol. 1, no. 10, pp. 838–844, 1985. DOI: [10.1179/026708385790123991](https://doi.org/10.1179/026708385790123991).
- [7] B. Buchmayr and J. S. Kirkaldy, "Modeling of the temperature field, transformation behavior, hardness and mechanical response of low alloy steels during cooling from the austenite region," *J. Heat Treating*, vol. 8, no. 2, pp. 127–136, 1990. DOI: [10.1007/BF02831633](https://doi.org/10.1007/BF02831633).
- [8] T. Reti, Z. Fried and I. Felde, "Computer simulation of steel quenching process using a multi-phase transformation model," *Comput. Mater. Sci.*, vol. 22, no. 3–4, pp. 261–278, 2001. DOI: [10.1016/S0927-0256\(01\)00240-3](https://doi.org/10.1016/S0927-0256(01)00240-3).

- [9] S. H. Kang and Y. T. Im, “Three-dimensional thermo-elastic – plastic finite element modeling of quenching process of plain-carbon steel in couple with phase transformation,” *Int. J. Mech. Sci.*, vol. 49, no. 4, pp. 423–439, 2007. DOI: [10.1016/j.ijmecsci.2006.09.014](https://doi.org/10.1016/j.ijmecsci.2006.09.014).
- [10] C. Şimşir and C. H. Gür, “A FEM based framework for simulation of thermal treatments: Application to steel quenching,” *Comput. Mater. Sci.*, vol. 44, no. 2, pp. 588–600, 2008. DOI: [10.1016/j.commatsci.2008.04.021](https://doi.org/10.1016/j.commatsci.2008.04.021).
- [11] D. Weisz-Patrault and T. Koedinger, “Residual stress on the run out table accounting for multiphase transitions and transformation induced plasticity,” *Appl. Math. Modell.*, vol. 60, pp. 18–33, 2018. doi:doi.org/10.1016/j.apm.2018.02.026. DOI: [10.1016/j.apm.2018.02.026](https://doi.org/10.1016/j.apm.2018.02.026).
- [12] J. Serri, M. Martiny and G. Ferron, “Finite element analysis of the effects of martensitic phase transformation in TRIP steel sheet forming,” *Int. J. Mech. Sci.*, vol. 47, no. 6, pp. 884–901, 2005. DOI: [10.1016/j.ijmecsci.2005.02.001](https://doi.org/10.1016/j.ijmecsci.2005.02.001).
- [13] P. Åkerström, G. Bergman and M. Oldenburg, “Numerical implementation of a constitutive model for simulation of hot stamping, Modelling and Simulation in,” *Modelling Simul. Mater. Sci. Eng.*, vol. 15, no. 2, pp. 105–119, 2007. DOI: [10.1088/0965-0393/15/2/007](https://doi.org/10.1088/0965-0393/15/2/007).
- [14] M. G. Lee, S. J. Kim, H. N. Han and W. C. Jeong, “Application of hot press forming process to manufacture an automotive part and its finite element analysis considering phase transformation plasticity,” *Int. J. Mech. Sci.*, vol. 51, no. 11–12, pp. 888–898, 2009. DOI: [10.1016/j.ijmecsci.2009.09.030](https://doi.org/10.1016/j.ijmecsci.2009.09.030).
- [15] P. Hippchen, A. Lipp, H. Grass, P. Craighero, M. Fleischer and M. Merklein, “Modelling kinetics of phase transformation for the indirect hot stamping process to focus on car body parts with tailored properties,” *J. Mater. Process. Technol.*, vol. 228, pp. 59–67, 2016. DOI: [10.1016/j.jmatprotec.2015.01.003](https://doi.org/10.1016/j.jmatprotec.2015.01.003).
- [16] M. Megahed, H. W. Mindt, N. N’Dri, H. Duan and O. Desmaison, “Metal additive-manufacturing process and residual stress modeling,” *Integr. Mater. Manuf. Innov.*, vol. 5, no. 1, pp. 61–93, 2016. DOI: [10.1186/s40192-016-0047-2](https://doi.org/10.1186/s40192-016-0047-2).
- [17] L. E. Lindgren, A. Lundbäck, M. Fisk, R. Pederson and J. Andersson, “Simulation of additive manufacturing using coupled constitutive and microstructure models,” *Additive Manufact.*, vol. 12, pp. 144–158, 2016. DOI: [10.1016/j.addma.2016.05.005](https://doi.org/10.1016/j.addma.2016.05.005).
- [18] Z. Luo and Y. Zhao, “A survey of finite element analysis of temperature and thermal stress fields in powder bed fusion Additive Manufacturing,” *Additive Manufact.*, vol. 21, no. March, pp. 318–332, 2018. DOI: [10.1016/j.addma.2018.03.022](https://doi.org/10.1016/j.addma.2018.03.022).
- [19] H. Huang, N. Ma, J. Chen, Z. Feng and H. Murakawa, “Toward large-scale simulation of residual stress and distortion in wire and arc additive manufacturing,” *Additive Manufact.*, vol. 34, pp. 101248, 2020. DOI: [10.1016/j.addma.2020.101248](https://doi.org/10.1016/j.addma.2020.101248).
- [20] D. Weisz-Patrault, “Fast simulation of temperature and phase transitions in directed energy deposition additive manufacturing,” *Additive Manufact.*, vol. 31, pp. 100990, 2020. doi: doi.org/10.1016/j.addma.2019.100990. DOI: [10.1016/j.addma.2019.100990](https://doi.org/10.1016/j.addma.2019.100990).
- [21] J. Jergéus, “Martensite formation and residual stresses around railway wheel flats,” *Proc. Instit. Mech. Engin., Part C: J. Mech. Engin. Sci.*, vol. 212, no. 1, pp. 69–79, 1998. DOI: [10.1243/0954406981521051](https://doi.org/10.1243/0954406981521051).
- [22] J. Ahlström, “Residual stresses generated by repeated local heating events – modelling of possible mechanisms for crack initiation,” *Wear*, vol. 366–367, no. Supplement C, pp. 180–187, 2016. DOI: [10.1016/j.wear.2016.05.029](https://doi.org/10.1016/j.wear.2016.05.029).
- [23] J. Ahlström and B. Karlsson, “Modelling of heat conduction and phase transformations during sliding of railway wheels,” *Wear*, vol. 253, no. 1–2, pp. 291–300, 2002. DOI: [10.1016/S0043-1648\(02\)00119-9](https://doi.org/10.1016/S0043-1648(02)00119-9).
- [24] J. Seo, S. Kwon, H. Jun and D. Lee, “Numerical stress analysis and rolling contact fatigue of White Etching Layer on rail steel,” *Int. J. Fatigue*, vol. 33, no. 2, pp. 203–211, 2011. DOI: [10.1016/j.ijfatigue.2010.08.007](https://doi.org/10.1016/j.ijfatigue.2010.08.007).
- [25] Q. Lian, G. Deng, H. Zhu, H. Li, X. Wang and Z. Liu, “Influence of white etching layer on rolling contact behavior at wheel-rail interface,” *Friction*, vol. 8, no. 6, pp. 1178–1196, 2020. DOI: [10.1007/s40544-020-0388-x](https://doi.org/10.1007/s40544-020-0388-x).
- [26] A. Esmaeili, J. Ahlström, B. Andersson and M. Ekh, “Modelling of cyclic plasticity and phase transformations during repeated local heating events in rail and wheel steels,” *Int. J. Fatigue*, vol. 151, pp. 106361, 2021. DOI: [10.1016/j.ijfatigue.2021.106361](https://doi.org/10.1016/j.ijfatigue.2021.106361).
- [27] T. Inoue and B. Raniecki, “Determination of thermal-hardening stress in steels by use of thermoplasticity theory,” *J. Mech. Phys. Solids*, vol. 26, no. 3, pp. 187–212, 1978. DOI: [10.1016/0022-5096\(78\)90008-X](https://doi.org/10.1016/0022-5096(78)90008-X).
- [28] S. Sjöström, “Interactions and constitutive models for calculating quench stresses in steel,” *Mater. Sci. Technol.*, vol. 1, no. 10, pp. 823–829, 1985. DOI: [10.1179/mst.1985.1.10.823](https://doi.org/10.1179/mst.1985.1.10.823).
- [29] J. Leblond, G. Mottet and J. Devaux, “A theoretical and numerical approach to the plastic behaviour of steels during phase transformations—I. derivation of general relations,” *J. Mech. Phys. Solids*, vol. 34, no. 4, pp. 395–409, 1986. DOI: [10.1016/0022-5096\(86\)90009-8](https://doi.org/10.1016/0022-5096(86)90009-8).
- [30] J. Leblond, G. Mottet and J. Devaux, “A theoretical and numerical approach to the plastic behaviour of steels during phase transformations—ii. study of classical plasticity for ideal-plastic phases,” *J. Mech. Phys. Solids*, vol. 34, no. 4, pp. 411–432, 1986. DOI: [10.1016/0022-5096\(86\)90010-4](https://doi.org/10.1016/0022-5096(86)90010-4).

- [31] S. Denis, S. Sjöström and A. Simon, “Coupled temperature, stress, phase transformation calculation model numerical illustration of the internal stresses evolution during cooling of a eutectoid carbon steel cylinder,” *MTA*, vol. 18, no. 7, pp. 1203–1212, 1987. DOI: [10.1007/BF02647190](https://doi.org/10.1007/BF02647190).
- [32] F. Fischer, G. Reissner, E. Werner, K. Tanaka, G. Cailletaud and T. Antretter, “A new view on transformation induced plasticity (trip),” *Int. J. Plast.*, vol. 16, no. 7–8, pp. 723–748, 2000. DOI: [10.1016/S0749-6419\(99\)00078-9](https://doi.org/10.1016/S0749-6419(99)00078-9).
- [33] H. Hallberg, P. Håkansson and M. Ristinmaa, “A constitutive model for the formation of martensite in austenitic steels under large strain plasticity,” *Int. J. Plast.*, vol. 23, no. 7, pp. 1213–1239, 2007. DOI: [10.1016/j.ijplas.2006.11.002](https://doi.org/10.1016/j.ijplas.2006.11.002).
- [34] T. Iwamoto and T. Tsuta, “Computational simulation on deformation behavior of ct specimens of trip steel under mode i loading for evaluation of fracture toughness,” *Int. J. Plast.*, vol. 18, no. 11, pp. 1583–1606, 2002. DOI: [10.1016/S0749-6419\(02\)00030-X](https://doi.org/10.1016/S0749-6419(02)00030-X).
- [35] R. Mahnken, A. Schneidt and T. Antretter, “Macro modelling and homogenization for transformation induced plasticity of a low-alloy steel,” *Int. J. Plast.*, vol. 25, no. 2, pp. 183–204, 2009. DOI: [10.1016/j.ijplas.2008.03.005](https://doi.org/10.1016/j.ijplas.2008.03.005).
- [36] M. Wolff, M. Böhm, R. Mahnken and B. Suhr, “Implementation of an algorithm for general material behavior of steel taking interaction of plasticity and transformation-induced plasticity into account,” *Int. J. Numer. Meth. Engng*, vol. 87, no. 12, pp. 1183–1206, 2011. DOI: [10.1002/nme.3154](https://doi.org/10.1002/nme.3154).
- [37] D. Weisz-Patrault, “Multiphase model for transformation induced plasticity. extended leblond’s model,” *J. Mech. Phys. Solids*, vol. 106, pp. 152–175, 2017. doi:doi.org/10.1016/j.jmps.2017.05.019. DOI: [10.1016/j.jmps.2017.05.019](https://doi.org/10.1016/j.jmps.2017.05.019).
- [38] M. Avrami, “Kinetics of phase change. I general theory,” *J. Chem. Phys.*, vol. 7, no. 12, pp. 1103–1112, 1939. DOI: [10.1063/1.1750380](https://doi.org/10.1063/1.1750380).
- [39] M. Avrami, “Kinetics of phase change. II Transformation-time relations for random distribution of nuclei,” *J. Chem. Phys.*, vol. 8, no. 2, pp. 212–224, 1940. DOI: [10.1063/1.1750631](https://doi.org/10.1063/1.1750631).
- [40] M. Avrami, “Granulation, phase change, and microstructure kinetics of phase change. III,” *J. Chem. Phys.*, vol. 9, no. 2, pp. 177–184, 1941. DOI: [10.1063/1.1750872](https://doi.org/10.1063/1.1750872).
- [41] D. Koistinen and R. Marburger, “A general equation prescribing the extent of the austenite-martensite transformation in pure iron-carbon alloys and plain carbon steels,” *Acta Metallurg.*, vol. 7, no. 1, pp. 59–60, 1959. DOI: [10.1016/0001-6160\(59\)90170-1](https://doi.org/10.1016/0001-6160(59)90170-1).
- [42] E. Scheil, “Anlaufzeit der austenitumwandlung,” *Archiv für das Eisenhüttenwesen*, vol. 8, no. 12, pp. 565–567, 1935. DOI: [10.1002/srin.193500186](https://doi.org/10.1002/srin.193500186).
- [43] G. W. Greenwood and R. Johnson, “The deformation of metals under small stresses during phase transformations,” *Proc. Roy. Soc. London. Series A. Math. Phys. Sci.*, vol. 283, no. 1394, pp. 403–422, 1965. DOI: [10.1098/rspa.1965.0029](https://doi.org/10.1098/rspa.1965.0029).
- [44] C. L. Magee, “Transformation kinetics, microplasticity and aging of martensite in Fe-31Ni,” Ph.D. thesis, Carnegie Institute of Technology, Pittsburgh, PA, 1966.
- [45] G. B. Olson and M. Cohen, “Kinetics of Strain-Induced Martensitic Nucleation,” *MTA*, vol. 6, no. 4, pp. 791–795, 1975. DOI: [10.1007/BF02672301](https://doi.org/10.1007/BF02672301).
- [46] H. Bhadeshia and D. Edmonds, “The mechanism of bainite formation in steels,” *Acta Metallurgica*, vol. 28, no. 9, pp. 1265–1273, 1980. DOI: [10.1016/0001-6160\(80\)90082-6](https://doi.org/10.1016/0001-6160(80)90082-6).
- [47] S. Petit-Grostabussiat, L. Taleb and J. F. Jullien, “Experimental results on classical plasticity of steels subjected to structural transformations,” *Int. J. Plast.*, vol. 20, no. 8–9, pp. 1371–1386, 2004. DOI: [10.1016/j.ijplas.2003.07.003](https://doi.org/10.1016/j.ijplas.2003.07.003).
- [48] V. Levitas, A. Idesman, G. Olson and E. Stein, “Numerical modelling of martensitic growth in an elastoplastic material, Philosophical Magazine,” *Part A*, vol. 82, no. 3, pp. 429–462, 2002. DOI: [10.1080/01418610208239609](https://doi.org/10.1080/01418610208239609).
- [49] R. Ostwald, T. Bartel and A. Menzel, “A one-dimensional computational model for the interaction of phase-transformations and plasticity,” *Int. J. Struct. Changes Solids*, vol. 3, no. 1, pp. 63–82, 2011.
- [50] R. Ostwald, T. Bartel and A. Menzel, “An energy-barrier-based computational micro-sphere model for phase-transformations interacting with plasticity,” *Comput. Methods Appl. Mech. Engin.*, vol. 293, pp. 232–265, 2015. DOI: [10.1016/j.cma.2015.04.008](https://doi.org/10.1016/j.cma.2015.04.008).
- [51] T. I. Zohdi and P. Wriggers, *An Introduction to Computational Micromechanics*, Vol. 20, Berlin: Springer Science & Business Media, 2004.
- [52] E. Arslan, W. Mack and T. Apatay, “Thermo-mechanically loaded steel/aluminum functionally graded spherical containers and pressure vessels,” *Int. J. Pressure Vessels Piping*, vol. 191, pp. 104334, 2021. DOI: [10.1016/j.ijpvp.2021.104334](https://doi.org/10.1016/j.ijpvp.2021.104334).
- [53] P. Spalthoff, W. Wunnike, C. Nauer-Gerhard, H. Bunge and E. Schneider, “Determination of the elastic tensor of a textured low-carbon steel,” *Texture Microstruct.*, vol. 21, no. 1, pp. 3–16, 1993. DOI: [10.1155/TSM.21.3](https://doi.org/10.1155/TSM.21.3).

- [54] O. Bouaziz and P. Buessler, "Iso-work increment assumption for heterogeneous material behavior modelling," *Adv. Eng. Mater.*, vol. 6, no. 12, pp. 79–83, 2004. DOI: [10.1002/adem.200300524](https://doi.org/10.1002/adem.200300524).
- [55] S. Golling, R. Östlund and M. Oldenburg, "A study on homogenization methods for steels with varying content of ferrite, bainite and martensite," *J. Mater. Process. Technol.*, vol. 228, pp. 88–97, 2016. DOI: [10.1016/j.jmatprotec.2015.07.007](https://doi.org/10.1016/j.jmatprotec.2015.07.007).
- [56] R. G. Stringfellow, D. M. Parks and G. B. Olson, "A constitutive model for transformation plasticity accompanying strain-induced martensitic transformations in metastable austenitic steels," *Acta Metallurgica Et Materialia*, vol. 40, no. 7, pp. 1703–1716, 1992. DOI: [10.1016/0956-7151\(92\)90114-T](https://doi.org/10.1016/0956-7151(92)90114-T).
- [57] S. Perdahcıoğlu and H. Geijselaers, "Constitutive modeling of two phase materials using the mean field method for homogenization," *Int. J. Mater. Form.*, vol. 4, no. 2, pp. 93–102, 2011. DOI: [10.1007/s12289-010-1007-6](https://doi.org/10.1007/s12289-010-1007-6).
- [58] C. Jessop, "Damage and defects in railway materials: Influence of mechanical and thermal damage on crack initiation and propagation," Ph.D. thesis, Chalmers University of Technology, Göteborg, 2019.
- [59] *BS EN 13674-1:2011 + A1:2017 Railway Applications. Track. Rail. Vignole Railway Rails 46 kg/m and above*. Brussels: European Committee for Standardization (CEN), 2011.
- [60] J. Orlich, A. Rose and P. Wiest, *Atlas Zur Wärmebehandlung Der Stähle, Band 3*. Düsseldorf: Max-Planck-Institut für Eisenforschung, 1973.
- [61] W. S. A. Rose, W. Peter and L. Rademacher, *Atlas Zur Wärmebehandlung Der Stähle, band 1, ii-101 a-f*. Düsseldorf: Max-Planck-Institut für Eisenforschung, Verlag Stahleisen, 1958.
- [62] C. Verdi and A. Visintin, "A mathematical model of the austenite-pearlite transformation in plain carbon steel based on the scheil's additivity rule," *Acta Metallurg.*, vol. 35, no. 11, pp. 2711–2717, 1987. DOI: [10.1016/0001-6160\(87\)90270-7](https://doi.org/10.1016/0001-6160(87)90270-7).
- [63] S. Denis, D. Farias and A. Simon, "Mathematical model coupling phase transformations and temperature evolutions in steels," *ISIJ Int.*, vol. 32, no. 3, pp. 316–325, 1992. DOI: [10.2355/isijinternational.32.316](https://doi.org/10.2355/isijinternational.32.316).
- [64] M. Wolff, M. Böhm and B. Suhr, "Comparison of different approaches to transformation-induced plasticity in steel," *Mat.-Wiss. u. Werkstofftech.*, vol. 40, no. 5–6, pp. 454–459, 2009. DOI: [10.1002/mawe.200900476](https://doi.org/10.1002/mawe.200900476).
- [65] J. Chaboche, "Constitutive equations for cyclic plasticity and cyclic viscoplasticity," *Int. J. Plast.*, vol. 5, no. 3, pp. 247–302, 1989. DOI: [10.1016/0749-6419\(89\)90015-6](https://doi.org/10.1016/0749-6419(89)90015-6).
- [66] C. O. Frederick and P. J. Armstrong, "A mathematical representation of the multiaxial Bauschinger effect," *Mat. at High Temp.*, vol. 24, no. 1, pp. 1–26, 2007. DOI: [10.1179/096034007X207589](https://doi.org/10.1179/096034007X207589).
- [67] M. Ekh, "Thermo-elastic-viscoplastic modeling of in792," *J. Mech. Behav. Mater.*, vol. 12, no. 6, pp. 359–388, 2001. DOI: [10.1515/JMBM.2001.12.6.359](https://doi.org/10.1515/JMBM.2001.12.6.359).
- [68] J. Hutchinson, "Elastic-plastic behaviour of polycrystalline metals and composites," *Proc. Roy. Soc. A: Math. Phys. Engin. Sci.*, vol. 319, pp. 247–272, 1970. DOI: [10.1098/rspa.1970.0177](https://doi.org/10.1098/rspa.1970.0177).
- [69] R. A. Lebensohn, P. A. Turner, J. W. Signorelli, G. R. Canova and C. N. Tomé, "Calculation of intergranular stresses based on a large-strain viscoplastic self-consistent polycrystal model, Modelling and Simulation in," *Modelling Simul. Mater. Sci. Eng.*, vol. 6, no. 4, pp. 447–465, 1998. DOI: [10.1088/0965-0393/6/4/011](https://doi.org/10.1088/0965-0393/6/4/011).
- [70] R. A. Lebensohn, C. N. Tomé and P. P. Castañeda, "Self-consistent modelling of the mechanical behaviour of viscoplastic polycrystals incorporating intragranular field fluctuations," *Philosophical Magazine*, vol. 87, no. 28, pp. 4287–4322, 2007. DOI: [10.1080/14786430701432619](https://doi.org/10.1080/14786430701432619).
- [71] S. Corp, *Abaqus Analysis User's Manual*, 2018th Edition, Providence, RI: Dassault Systèmes, 2018.
- [72] C. Jessop, J. Ahlström, C. Persson and Y. Zhang, "Damage evolution around white etching layer during uniaxial loading," *Fatigue Fract. Eng. Mater. Struct.*, vol. 43, no. 1, pp. 201–208, 2020. DOI: [10.1111/ffe.13044](https://doi.org/10.1111/ffe.13044).
- [73] J. Ahlström and B. Karlsson, "Analytical 1D model for analysis of the thermally affected zone formed during railway wheel skid," *Wear*, vol. 232, no. 1, pp. 15–24, 1999. DOI: [10.1016/S0043-1648\(99\)00167-2](https://doi.org/10.1016/S0043-1648(99)00167-2).
- [74] S. Software, Jmatpro 6.0, 2018. <https://www.sentsoftware.co.uk/jmatpro>
- [75] *Railway applications - Wheelsets and bogies - Wheels - Product Requirement*. EN 13262:2004 + A1, Brussels: European Committee for Standardization (CEN), 2004.
- [76] C. Şimşir and C. H. Gür, "A simulation of the quenching process for predicting temperature, microstructure and residual stresses," *Strojnicki Vestnik/J. Mech. Engin.*, vol. 56, no. 2, pp. 93–103, 2010.